



Constraints on r -modes and Mountains on Millisecond Neutron Stars in Binary Systems

P. B. Covas¹ , M. A. Papa¹ , R. Prix¹ , and B. J. Owen² ¹ Max Planck Institute for Gravitational Physics (Albert Einstein Institute) and Leibniz Universität Hannover D-30167 Hannover, Germany; pep.covas.vidal@aei.mpg.de, maria.alessandra.papa@aei.mpg.de, reinhard.prix@aei.mpg.de² Department of Physics and Astronomy, Texas Tech University, Lubbock, TX, 79409-1051, USA; benjamin.b.owen@ttu.edu

Received 2022 March 4; revised 2022 March 29; accepted 2022 March 30; published 2022 April 19

Abstract

Continuous gravitational waves are nearly monochromatic signals emitted by asymmetries in rotating neutron stars. These signals have not yet been detected. Deep all-sky searches for continuous gravitational waves from isolated neutron stars require significant computational expense. Deep searches for neutron stars in binary systems are even more expensive, but these targets are potentially more promising emitters, especially in the hundreds of Hertz region, where ground-based gravitational-wave detectors are most sensitive. We present here an all-sky search for continuous signals with frequency between 300 and 500 Hz, from neutron stars in binary systems with orbital periods between 15 and 60 days and projected semimajor axes between 10 and 40 lt-s. This is the only binary search on Advanced LIGO data that probes this frequency range. Compared to previous results, our search is over an order of magnitude more sensitive. We do not detect any signals, but our results exclude plausible and unexplored neutron star configurations, for example, neutron stars with relative deformations greater than 3×10^{-6} within 1 kpc from Earth and r -mode emission at the level of $\alpha \sim$ a few 10^{-4} within the same distance.

Unified Astronomy Thesaurus concepts: Gravitational waves (678); Neutron stars (1108)

Supporting material: data behind figure

1. Introduction

Detecting continuous gravitational waves is one of the most anticipated milestones in gravitational-wave astronomy. In spite of much effort, no detection has been achieved yet (Fesik & Papa 2020; Abbott et al. 2021a, 2021b, 2021c, 2021d; Ashok et al. 2021; Dergachev & Papa 2021; Rajbhandari et al. 2021; Steltner et al. 2021; Zhang et al. 2021; Abbott et al. 2022a, 2022b; Ming et al. 2022).

Continuous gravitational-wave signals can be produced by asymmetric rotating neutron stars due to

1. a mountain, i.e., a nonaxisymmetric deformation rigidly rotating with the star. If the principal moment of inertia is aligned with the spin axis of the star, this generates gravitational waves at a frequency $f = 2\nu$, where ν is the rotational frequency of the neutron star.
2. r -modes, a long-lasting oscillation mode that generates gravitational waves at a frequency of approximately $f \sim 4\nu/3$, with the exact relationship depending on the details of the neutron star equation of state (Yoshida et al. 2005; Idrisy et al. 2015).

Other mechanisms also exist, most notably following a glitch in the neutron star spin (see van Eysden & Melatos 2008 and references therein), but we will not consider them here.

The mountain asymmetry could be generated by strains in the crust of the star, by internal magnetic fields, or by accretion from a companion star (see for example Lasky 2015; Glampedakis & Gualtieri 2018). Most theoretical studies in the literature (e.g., Owen 2005) provide upper limits on the possible mountain height, while there are few concrete models

(Singh et al. 2020a) predicting physical mechanisms that would actually produce such long-lasting mountains.

On the other hand, r -modes in rotating neutron stars are unstable to gravitational-wave emission (Andersson 1998; Friedman & Morsink 1998; Lindblom et al. 1998; Owen et al. 1998). The instability is counteracted only by dissipative mechanisms in the neutron star such as viscosity, crust-core boundary friction, or through nonlinear mode coupling (e.g., see Bondarescu et al. 2007, 2009; Bondarescu & Wasserman 2013). This leads to predictions of the so-called (in)stability window, i.e., ranges of the neutron star parameters where the r -modes are (un)stable. There are large theoretical uncertainties on the details of the r -mode stability window, amplitude, and timescales, but several studies predict that long-lasting r -modes are present in accreting or post-accretion (quiescent) neutron stars in low-mass X-ray binaries (qLMXBs) (Andersson et al. 1999; Reisenegger & Bonacic 2003).

Furthermore, some authors (e.g., Chugunov et al. 2014; Maccarone et al. 2022) argue for the existence of a potentially large unobserved population of quiescent LMXBs that may be subject to long-lasting ($\sim 10^9$ yr) r -mode emission. These models provide compelling astrophysical motivation for an all-sky search for unknown neutron stars in binary systems emitting continuous gravitational waves. In turn, nonobservation of such signals can potentially provide astrophysically relevant and informative upper limits, especially on r -mode amplitudes.

Independently of the emission mechanism, the expected continuous-wave amplitude is many orders of magnitude lower than the average noise level, so that months or years of data have to be combined together in order to build up a detectable signal-to-noise ratio.

The frequency of these signals is usually described in the source frame by an $n = 1$ or $n = 2$ order Taylor expansion around a reference time (referred to as ITn signals in Dergachev & Papa 2021). This means that in the source frame, two or



Original content from this work may be used under the terms of the [Creative Commons Attribution 4.0 licence](https://creativecommons.org/licenses/by/4.0/). Any further distribution of this work must maintain attribution to the author(s) and the title of the work, journal citation and DOI.

three parameters are needed to describe the frequency evolution of the signal. In the observer frame, amplitude and Doppler modulations need to be accounted for in order to accurately describe the signal frequency evolution, which means that now, the sky position of the source needs to be specified (two more parameters). Searching for signals from neutron stars with known parameters does not pose any difficulty because this amounts to a single waveform, which in the observer frame is specified by the value of four or five parameters. But for unknown sources, the high resolution in all the parameters makes the all-sky, broad frequency searches the most computationally costly among all gravitational-wave searches. A recent review of different methods to perform these searches can be found in Tenorio et al. (2021).

If the unknown neutron star is assumed to be in a binary system rather than being isolated, the search problem becomes even more difficult. Assuming a circular orbit, three additional parameters need to be accounted for, which further increases the already high computational cost of all-sky surveys. However, because more than half of the known millisecond pulsars are in binary systems and their accretion history offers channels to generate the asymmetries needed for a detectable continuous signal (Chugunov et al. 2014; Holgado et al. 2018; Gittins & Andersson 2019; Singh et al. 2020b), searches for signals from unknown neutron stars in binaries are very interesting.

In this paper we present the results of an all-sky search for continuous waves from neutron stars in binary systems with gravitational-wave frequencies between 300 and 500 Hz, using the public Advanced LIGO O3a data (LVC 2021). This search complements two previous Advanced LIGO data searches, which looked at frequencies between 50 and 300 Hz (Covas & Sintes 2020; Abbott et al. 2021d). The frequency range up to 500 Hz was previously explored using S6 and VSR2/3 data (Aasi et al. 2014), producing upper limits on the gravitational-wave amplitude that are not more stringent than $\sim 7.5 \times 10^{-24}$. Our search improves on these results by nearly a factor of 30, with our most restrictive upper limit being $\sim 2.8 \times 10^{-25}$.

We search for signals from systems with a projected semimajor axis between 10 and 40 lt-s and orbital periods between 15 and 60 days. These parameter ranges are very similar to the ones searched by Covas & Sintes (2020) and in region A of Abbott et al. (2021d), the difference being that we have extended the largest orbital period from 45 to 60 days. The previous search using S6 and VSR2/3 data (Aasi et al. 2014) explored a wider range of parameter space, covering orbital periods from 0.08 to 94 days.

We use a newly developed search pipeline—BinarySkyHou \mathcal{F} —which combines coherent \mathcal{F} -statistic search results with the Hough transform method (Krishnan et al. 2004; Covas & Sintes 2019). BinarySkyHou \mathcal{F} is an improvement over the method of Covas & Sintes (2019), due to its lower computational cost and the usage of a generally more sensitive coherent detection statistic (P. B. Covas 2022, in preparation).

The paper is organized as follows: In Section 2, we describe the data that we use; in Section 3 we briefly explain the search method; and in Section 4 we present results and discuss their astrophysical implications, which we summarize in Section 5.

2. Data

This search uses the Advanced LIGO O3a data (LVC 2021). O3a comprises the first 6 months of the O3 run, i.e., 2019 April–October, and is the first O3 data set publicly released.

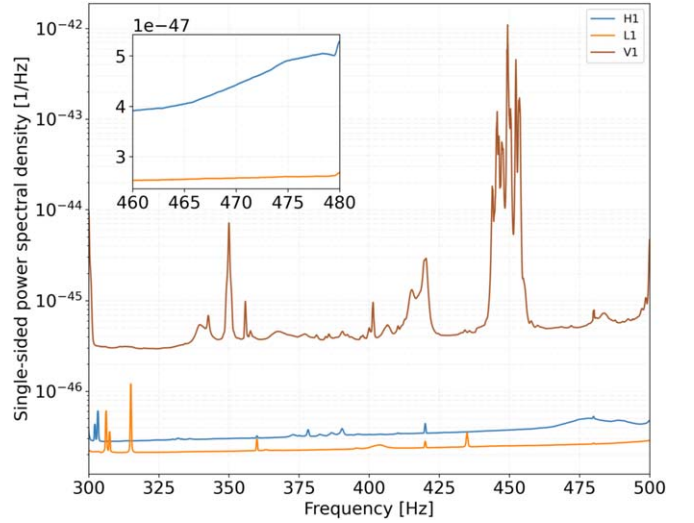


Figure 1. Power spectral density S_n , harmonically averaged over SFTs, for the three detectors as a function of frequency. The inset shows the region around the surviving outlier of the follow-up.

We use data from both LIGO gravitational-wave detectors, i.e., from the Hanford (H1) and the Livingston (L1) detectors (Aasi et al. 2015). We do not consider data from the Virgo detector because the amplitude spectral density is ~ 3 times higher than that of LIGO and is more contaminated by non-Gaussian disturbances. The harmonic average power spectral density of the LIGO and Virgo detectors in the frequency range covered by this search is shown in Figure 1.

We use the GWOSC-16KHZ_R1_STRAIN channel and the DCS-CALIB_STRAIN_CLEAN_SUB60HZ_C01_AR frame type. These data had been cleaned before public release at the frequencies of the power 60 Hz lines and the calibration lines. Many other lines are still present in the data set, producing spurious outliers that need to be examined and discarded, as will be seen in Section 4.

As discussed in other publications (e.g., Abbott et al. 2022a), the O3a data set suffers from a large number of short-duration glitches that increase the noise level in the frequency range of interest for this search, thus potentially reducing the sensitivity. For this reason, we use the gating method developed by Steltner et al. (2022) to remove these glitches and improve the data quality.

The data set of each detector is divided into short Fourier transforms (SFTs; see Allen & Mendell 2004) of 200 s, which is short enough that the signal power does not spread by more than a 1/200 Hz frequency bin during this time. In fact, in the chosen range of orbital and frequency parameters, this remains the case for durations up to ≈ 1200 s (see Figure 8 of Covas & Sintes 2019). The total number of SFTs is 55,068 for H1 and 56,118 for L1.

3. The Search

3.1. Signal Model

The gravitational-wave signal $h(t)$ from a triaxial asymmetric rotating neutron star as a function of time t in the observer frame is given by Jaranowski et al. (1998):

$$h(t) = h_0 \left[F_+(t; \psi) \frac{1 + \cos^2 \iota}{2} \cos[\phi_0 + \phi(t)] + F_\times(t; \psi) \cos \iota \sin[\phi_0 + \phi(t)] \right], \quad (1)$$

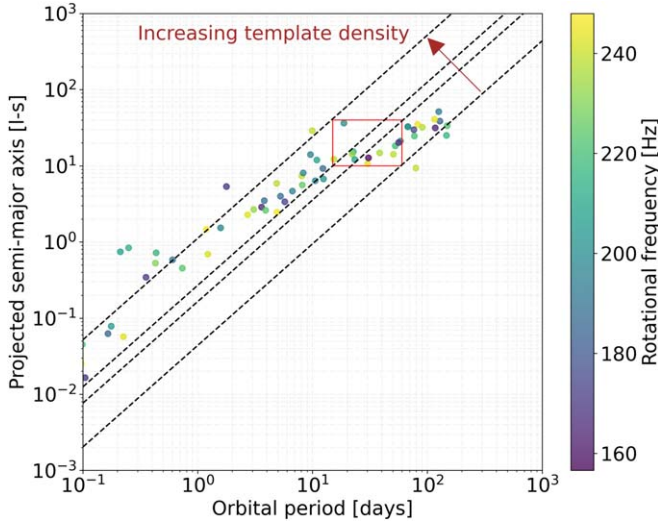


Figure 2. The red box shows the parameter space covered by this search, while the points show the population of known pulsars in binary systems with rotational frequencies between 150 and 250 Hz. The dashed black lines indicate points of equal template density.

where F_+ and F_\times are the antenna-pattern functions of the detector, ι is the inclination angle of the angular momentum of the source with respect to the line of sight, ψ is the polarization angle, ϕ_0 is the initial phase, $\phi(t)$ is the gravitational-wave phase at time t , and h_0 is the intrinsic gravitational-wave amplitude.

The phase of the signal $\phi(t)$ in the observer frame depends on the intrinsic frequency f_0 and frequency derivatives of the signal and on the Doppler modulation of this signal due to the relative motion between the source and the detector. The Doppler modulation depends on the gravitational-wave frequency, the sky position of the source (α and δ), and the parameters describing the Keplerian orbit of the neutron star. These orbital parameters are orbital period P , projected orbital semimajor axis a_p , time of ascension t_{asc} , argument of periaapsis, and eccentricity. In an all-sky search for IT1 signals, this in principle amounts to nine parameters to be searched for, in order to accurately track the signal.

3.2. Parameter Space Covered

We search for signals with intrinsic frequency f_0 between 300 and 500 Hz and frequency derivative $|\dot{f}_0| \leq 4 \times 10^{-10}$ Hz/s across the entire sky. We choose this frequency range because it has not yet been covered by a search on Advanced LIGO data. The chosen frequency derivative range allows us to set all template waveforms $\dot{f}_0 = 0$ and hence not to search over multiple different frequency derivative values in the first stage of the search. With this range we are able to cover the expected frequency derivative values produced by spin wandering, which may appear in accreting systems (Mukherjee et al. 2018).

We assume that the signals come from a neutron star in a binary system. As shown in Figure 2, neutron stars in binary systems cover a broad range of orbital separations a_p , depending on the neutron star companion mass and on the orbital period. On the other hand, all-sky high-sensitivity/high-resolution searches over such a broad range of orbital parameters are impossible due to their computational cost, so we concentrate the search in the range of P – a_p indicated by the

Table 1

Range of Values of the Signal Waveform Parameters Covered by the Search

| Parameter | Range |
|--|--|
| f_0 : Frequency [Hz] | 300–500 |
| $ \dot{f}_0 $: Frequency deriv. [Hz/s] | $< 4 \times 10^{-10}$ |
| a_p : Projected semimajor axis [lt-s] | 10–40 |
| P : Orbital period [days] | 15–60 |
| t_{asc} : Time of ascension [s] | $t_m \pm P/2$ |
| e : Orbital eccentricity | $< 5.7 \times 10^{-3} \left[\frac{500 \text{ Hz}}{f_0} \right]$ |
| α : Right ascension [rad] | 0– 2π |
| δ : decl. [rad] | $-\pi/2$ – $\pi/2$ |

Note. As explained in the text, in order to cover the first frequency derivative \dot{f}_0 and the eccentricity e ranges, we only search a single template. For this reason, we do not quote a grid resolution for these two parameters in Table 2. t_m is the midtime of the search.

red box in Figure 2. This box is chosen in such a way that, among the search boxes that could be drawn in that plane with the same computational cost for the associated search, this box contains the highest number of pulsars in it, while probing higher orbital periods than previous searches on Advanced LIGO data (Abbott et al. 2021d). To give some idea of how the computational cost varies in the a_p – P plane, we also plot lines of constant template-count density (from Equation (77) of Leaci & Prix 2015). Following Covas & Sintes (2019) we assume an orbital eccentricity smaller than $5.7 \times 10^{-3} \left[\frac{500 \text{ Hz}}{f_0} \right]$, so in the first stage of the search we set all template waveforms $e = 0$ and do not search over different eccentricity (and argument of periaapsis) values.

The signal parameter space covered by the search is summarized in Table 1. The total number of templates searched is $\sim 6 \times 10^{14}$.

3.3. Summary of the Pipeline

We use a semicoherent search method, where the data are separated into segments of a maximum span $T_{\text{seg}} = 900$ s. For all segments, we calculate the coherent detection statistic \mathcal{F} of Cutler & Schutz (2005) and Jaranowski et al. (1998) over a coarse grid in frequency and sky. The segment length T_{seg} is short enough that the orbital parameters are not resolved. The \mathcal{F} -statistic values are then combined with an improved version of the BinarySkyHough methodology of Covas & Sintes (2019), described in more detail in P. B. Covas (2022, in preparation). By using the \mathcal{F} -statistic, the new pipeline can leverage sensitivity gains from the use of longer coherent duration segments and from the coherent combination of data from different detectors. However, with the particular setup used for this search—short segment length and two detectors—its sensitivity is comparable to that of power-based statistics.

The final detection statistic is a weighted sum of the single-segment statistic \mathcal{F}_i :

$$2\mathcal{F}_{\text{sum}} = \sum_{i=1}^{N_{\text{seg}}} w_i 2\mathcal{F}_i, \quad (2)$$

where w_i depends on the detectors' antenna beam-pattern functions during segment i , inverse-weighted with the noise power spectral density, and $N_{\text{seg}} = 16,966$. The sum of Equation (2) depends on the template orbital parameters.

Table 2
Grid Resolutions in the Various Waveform Parameters

| Resolution | Frequency Range | |
|--|--|--|
| | [300, 400) | [400, 500) |
| δf_0 [mHz] | 1.1 | 1.1 |
| δa_p [l-s] | $\left[\frac{P}{37 \text{ days}} \right]$ | $\left[\frac{P}{37 \text{ days}} \right]$ |
| $\delta \Omega$ [10^{-8} rad] | $\left[\frac{P}{37 \text{ days}} \right] \left[\frac{25 \text{ l-s}}{a_p} \right]$ | $\left[\frac{P}{37 \text{ days}} \right] \left[\frac{25 \text{ l-s}}{a_p} \right]$ |
| δt_{asc} [10^4 s] | $\left[\frac{P}{37 \text{ days}} \right]^2 \left[\frac{25 \text{ l-s}}{a_p} \right]$ | $\left[\frac{P}{37 \text{ days}} \right]^2 \left[\frac{25 \text{ l-s}}{a_p} \right]$ |
| $\delta \alpha = \delta \delta$ [10^{-2} rad] | 4.3 | 4.0 |

Note. $\Omega = 2\pi/P$ is the average angular orbital velocity.

We use the coherent detection statistic \mathcal{F} for all segments that have a well-conditioned antenna-pattern matrix with condition number $< 10^4$. For larger condition numbers, the \mathcal{F} -statistic becomes numerically singular, and we use the constant antenna-pattern detection statistic with two degrees of freedom derived in Covas & Prix (2022).

We divide the search into a low- and a high-frequency region, each 100 Hz wide, and use different template grids in order to balance the computational cost in the two regions. The grid resolutions for all the parameters are shown in Table 2. The overall resulting average mismatch is $\lesssim 0.6$, and the mismatch distributions at four frequencies spanning the search range are shown in Figure 3.

We define a significance s for every search result as

$$s = \frac{2\mathcal{F}_{\text{sum}} - \mu}{\sigma}, \quad (3)$$

where

$$\mu = 4 \sum_{i=1}^{N_4} w_{4;i} + 2 \sum_{j=1}^{N_2} w_{2;j}, \quad (4)$$

$$\sigma^2 = 2 \left(4 \sum_{i=1}^{N_4} w_{4;i}^2 + 2 \sum_{j=1}^{N_2} w_{2;j}^2 \right), \quad (5)$$

are the mean and standard deviation of $2\mathcal{F}_{\text{sum}}$ in Gaussian noise, and $w_{4;i}$ ($w_{2;j}$) are the weights for the N_4 (N_2) segments with four (two) degrees of freedom, respectively.

4. Results

4.1. Outliers, Follow-up

We consider the most significant 5×10^5 results in every 0.1 Hz band, which are shown in Figure 4. On these, we use the clustering procedure of Covas & Sintes (2019, 2020) and group together results due to the same cause. The top 10 clusters per 0.1 Hz band are saved for further analysis, yielding a total of 20,000 clusters. In what follows we will refer to these selected clusters as candidates.

Before analyzing the candidates with a longer coherence time, we search for the presence of instrumental lines in their vicinity. We use the list of LIGO detectors' lines compiled by Goetz et al. (2021). We calculate the frequency-time pattern of

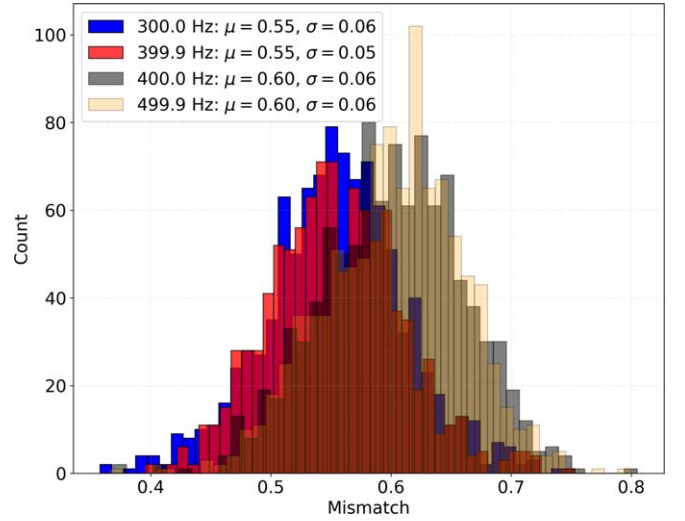


Figure 3. The mismatch distribution of this search at four frequencies, with the other parameters spanning the ranges given in Table 1, as explained in the text.

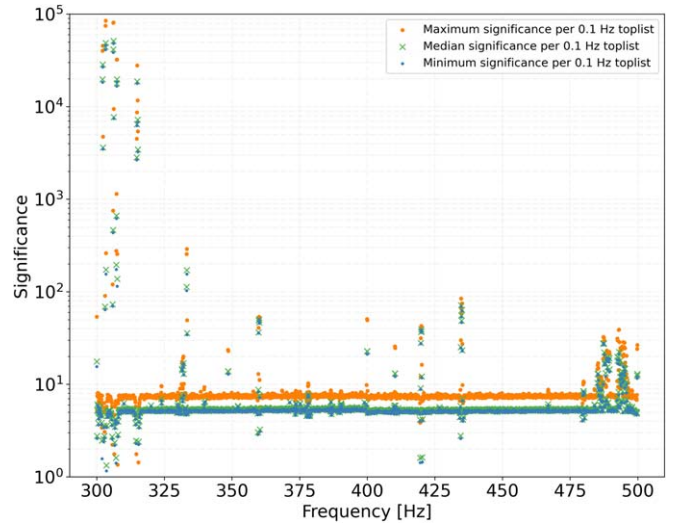


Figure 4. Significance of the top 5×10^5 candidates in each 0.1 Hz frequency band. We show the maximum, median, and minimum values. The lower-than-average values of the significance are due to the σ from Equation (5) being an overestimate of the actual standard deviation because of the noise weight being higher in the vicinity of a noise disturbance.

every candidate and discard it if it crosses any of the lines in the lists. Doing this, 19,044 candidates remain.

In the next step, we apply the same follow-up that was used in Covas & Sintes (2020), where we increase the coherence time (T_{seg}) to 9000 s and use a Markov Chain Monte Carlo (MCMC) procedure to calculate the detection statistic (Ashton et al. 2020; Keitel et al. 2021). Due to the significantly longer coherent time baseline of the follow-up, the detection statistic $2\mathcal{F}$ is an average of the detection statistics from each of the 1728 segments, without any noise weights. Furthermore, due to the increase in coherence time, the follow-up resolves different values of the argument of periaapsis, eccentricity, and frequency derivative, which now need to be all searched for explicitly.

If one of our MCMC candidates is due to a gravitational-wave signal, its detection statistic value must be consistent with what is expected from a signal. This is shown in Figure 5, where we have the distribution of detection statistic values after the MCMC follow-up of 4763 candidates stemming from fake

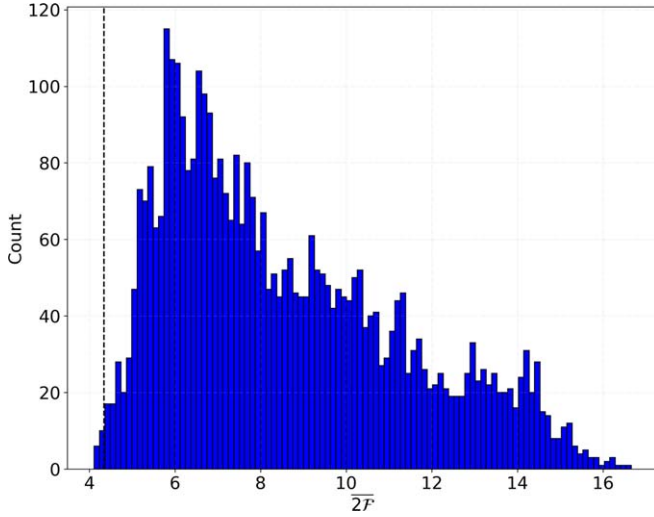


Figure 5. Distribution of $\overline{2\mathcal{F}}$ values (averaged over segments) from the MCMC follow-up of 4763 fake signals that survive the initial stage of our search.

signals added to the O3a data. The signal parameters are distributed within the ranges of Table 1.³ Each of the 4763 candidates has passed the previous stage of the search, i.e., is one of the top 10 clusters in its 0.1 Hz band. The amplitudes of the fake signals bracket the 95% upper-limit value. Based on the distribution of recovered values, we set a threshold for our MCMC candidates at $\overline{2\mathcal{F}}_{\text{thr}} = 4.34$, which corresponds to about a 1% false dismissal rate.

The distribution of $\overline{2\mathcal{F}}$ for our candidates is shown in Figure 6: Only one candidate out of the 19,044 survives, at $f_0 \sim 466.93$ Hz. We investigate the candidate by performing single-detector searches with the same setup as the initial search. This reveals higher detection statistic values from the H1 detector over a too broad range of frequencies (~ 0.3 Hz) to be consistent with an astrophysical signal (see Figure 7). Even though this spectral region does not display significant disturbances (see inset of Figure 1) and no line is present in the line list (Goetz et al. 2021), the fact that the high detection statistic value comes from the least sensitive detector further supports the idea that it is not of astrophysical origin. Additionally, we perform a $T_{\text{seg}} = 3600$ s dedicated `BinarySkyHou` \mathcal{F} follow-up of this candidate with only L1 data (i.e., the undisturbed data), and the resulting detection statistic falls short of what is expected for a signal. Therefore, no candidates survive the follow-up stage.

We note that no hardware injections (artificially added signals) are present in the frequency range covered by this search, so we do not expect any surviving candidates from hardware-injected signals.

4.2. Upper Limits

We calculate the 95% confidence upper limits on the intrinsic gravitational-wave amplitude $h_0^{95\%}(f_0)$ in every 0.1 Hz band. This is the amplitude such that 95% of a population of signals with frequency in that band and with the values of the other parameters in our search range would have been detected.

³ The cosine of the source inclination angle, the polarization angle, the initial phase, the frequency, the orbital period, the projected semimajor axis, the log of the eccentricity, and the frequency derivative are uniformly distributed; sky positions are isotropically distributed in the sky.

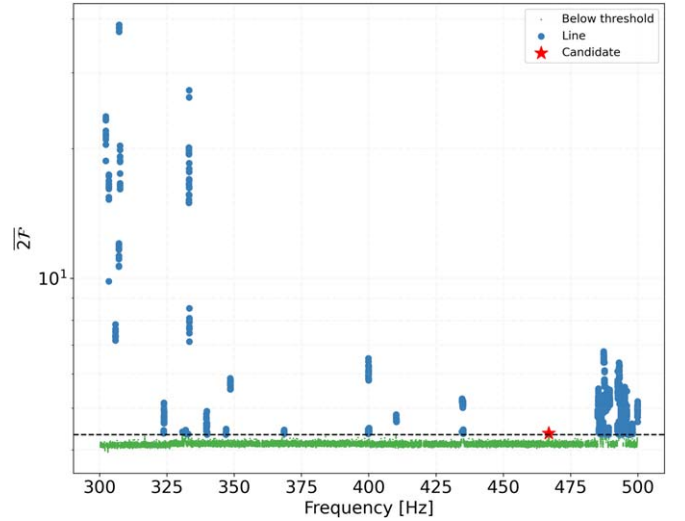


Figure 6. $\overline{2\mathcal{F}}$ values for each of the 19,044 candidates followed-up with the MCMC procedure as a function of the frequency of the candidate signals. The horizontal threshold line is the threshold value at $\overline{2\mathcal{F}}_{\text{thr}} = 4.34$.

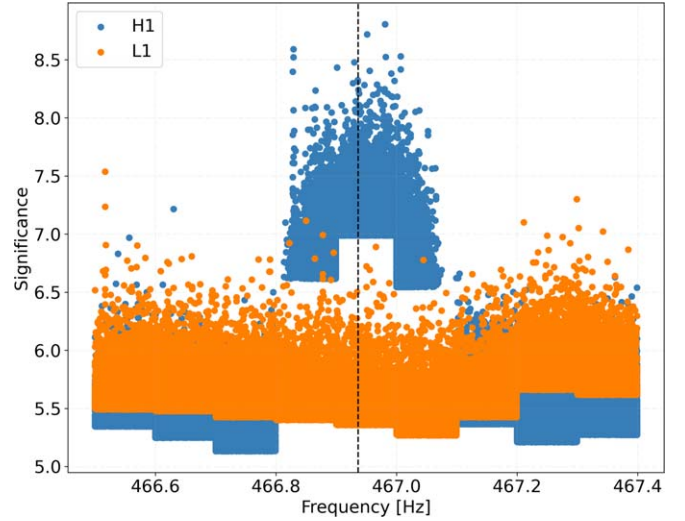


Figure 7. Significance values around the candidate at 466.93 Hz when analyzing only H1 or L1 data. The vertical dashed line marks the frequency of the outlier that survives the follow-up stage.

The detection criterion for a signal is that it makes it in the top 10 list for the relevant band and that it passes the MCMC output threshold.

We determine the $h_0^{95\%}(f_0)$ in four representative 0.1 Hz bands in the lower- and upper-frequency regions. In each band, we compute the percentage of detected signals from 500 search-and-recoveries, with signals added to the data at a fixed value of h_0 . This is a standard procedure, recently also employed by Abbott et al. (2021d), Covas & Sintes (2020), and Steltner et al. (2021).

We can associate with each 0.1 Hz upper limit a corresponding sensitivity depth \mathcal{D} (Behnke et al. 2015; Dreissigacker et al. 2018), defined as

$$\mathcal{D}^{95\%}(f) = \frac{\sqrt{S_n(f)}}{h_0^{95\%}}, \quad (6)$$

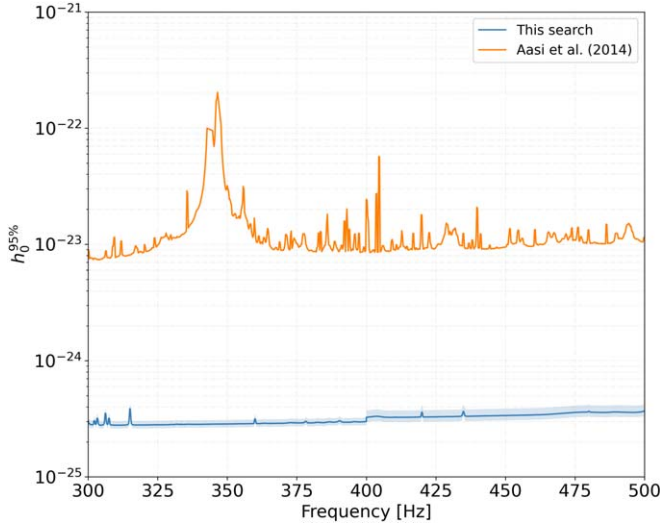


Figure 8. Upper limits on the gravitational-wave amplitude $h_0^{95\%}$. The lower blue curve shows the results for this search (with the shaded area showing the 1σ confidence region), while the upper orange curve shows the S6 data results of Aasi et al. (2014), the only previous search covering this frequency range. The slight discontinuity at 400 Hz is due to the change in the search grid spacings, as shown in Table 2. The upper-limit values are available as data behind the figure.

(The data used to create this figure are available.)

where $S_n(f)$ is the power spectral density of the data. In reasonably well-behaved noise, this quantity does not vary much with frequency and is a good measure of the sensitivity of the search because it quantifies how far below the noise floor the smallest detectable signal lies. The average sensitivity depth for the low- and high-frequency band of Table 2 is $17.6^{+1.3}_{-1.4}$ [1/ $\sqrt{\text{Hz}}$] and $16.2^{+1.7}_{-1.9}$ [1/ $\sqrt{\text{Hz}}$], respectively, with the 1σ uncertainties. We use these sensitivity depth values as scale factors to determine the upper limits in the remaining bands from measurements of the noise floor S_n . The upper-limit values in machine-readable format are available as data behind the figure.⁴

The results of this procedure are shown in Figure 8. The most sensitive upper limit is 2.8×10^{-25} at 311.7 Hz. Compared with the only previous search that analyzed this region of parameter space using S6 data (Aasi et al. 2014), this search is over 27 times more sensitive, due to the more sensitive data set and a more sensitive pipeline. Abbott et al. (2021d) also searched O3a data (but only up to 300 Hz) and attained a sensitivity comparable to ours.

4.3. Astrophysical Reach

The gravitational-wave amplitude emitted due to an equatorial ellipticity ϵ is

$$h_0 = \frac{4\pi^2 G}{c^4} \frac{I_{zz} \epsilon f_0^2}{d}, \quad (7)$$

where $\epsilon = |I_{xx} - I_{yy}|/I_{zz}$, I_{zz} is the moment of inertia of the star with respect to the principal axis aligned with the rotation axis,

⁴ Upper-limit values in machine-readable format are also available at <https://www.aci.mpg.de/continuouswaves/O3aAllSkyBinary>.

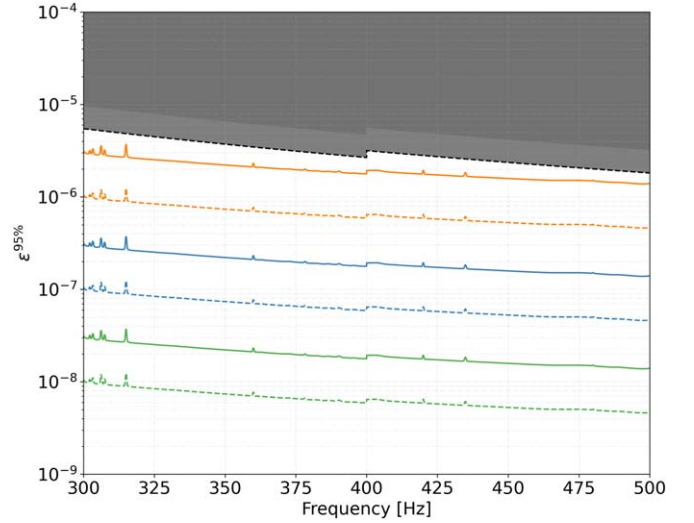


Figure 9. Upper limits on the neutron star ellipticity ϵ at the 95% confidence level. The three different colors show results for distances of 1 kpc (upper orange curves), 100 pc (middle blue curves), and 10 pc (green bottom curves). The dashed lines use a moment of inertia of $I_{zz} = 3 \times 10^{38} \text{ kg m}^2$ instead of the canonical $I_{zz} = 10^{38} \text{ kg m}^2$ value, used by the solid lines. In the upper shaded gray area, this search is not sensitive because the high ellipticities would generate a spin-down larger than this search can probe.

d is the distance, and f_0 is the gravitational-wave frequency, which in this model is equal to twice the rotational frequency.

The upper limits on h_0 can hence be used to calculate upper limits on the asymmetry of the targeted neutron star population by rearranging Equation (7). These ellipticity upper limits depend on choosing a value for the unknown moment of inertia of the neutron star, which is uncertain by around a factor of 3 (see Section 4B of Abbott et al. 2007), although more exotic neutron star models such as quark stars or lower-mass neutron stars could have even higher moments of inertia (Owen 2005; Horowitz 2010). Figure 9 shows these results at three different distances and two values of the moment of inertia.

These upper limits on the ellipticity are the most restrictive to date for searches of unknown neutron stars in binary systems. If the true minimum ellipticity is 10^{-9} as suggested by some studies (such as Woan et al. 2018; Gittins & Andersson 2019), we are about one order of magnitude above that limit for neutron stars at 10 pc and two orders of magnitude for stars at 100 pc. For sources at 1 kpc, with $I_{zz} = 10^{38} \text{ kg m}^2$ and emitting continuous waves at 500 Hz, the ellipticity can be constrained at $\epsilon < 1.5 \times 10^{-6}$, while at 10 pc we have $\epsilon < 1.5 \times 10^{-8}$. If we assume $I_{zz} = 3 \times 10^{38} \text{ kg m}^2$ (as could be due to an equation of state that supports neutron stars with larger radii), the upper limits are more stringent, as shown by the dashed traces. For example, at 100 pc and 500 Hz, the upper limit is around a factor of 60 from the claimed minimum at 10^{-9} .

An alternative way to present these upper limits is to use the quadrupole moment Q_{22} , which is directly related to the ϵI_{zz} product:

$$Q_{22} = \sqrt{\frac{15}{8\pi}} \epsilon I_{zz} \rightarrow Q_{22}^{95\%} = \sqrt{\frac{15}{128\pi^5}} \frac{c^4}{G} \frac{h_0^{95\%}}{f_0^2} d. \quad (8)$$

By using the quadrupole, there is no need to choose a value for the moment of inertia I_{zz} . We can compare these upper limits on the quadrupole moment with the results obtained in

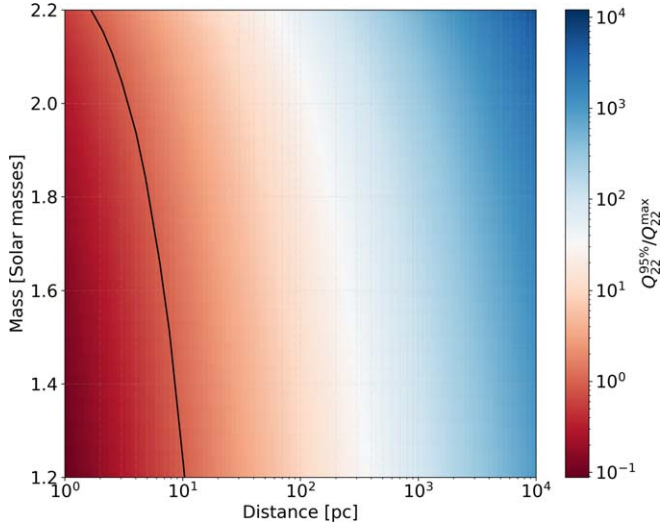


Figure 10. Ratio between our quadrupole moment upper limits $Q_{22}^{95\%}$ and the maximum quadrupole from the upper curve in Figure 1 of Gittins & Andersson (2021). The black line marks $Q_{22}^{95\%}/Q_{22}^{\max} = 1$, therefore our upper limits are constraining with respect to the model of Gittins & Andersson (2021) in the region to the left of this line.

Gittins & Andersson (2021), where the maximum quadrupole moment attainable by a neutron star with a certain mass was calculated. In this way, instead of plotting the absolute upper-limit value reached by our search, we can show the ratio by which our search is constraining the maximum value, in a similar way to what is done in targeted continuous gravitational-wave searches where the gravitational-wave amplitude spin-down limit is used (Ashok et al. 2021).

This result can be seen in Figure 10, where the color indicates the ratio between the calculated upper limits and the maximum quadrupole of Gittins & Andersson (2021) for a 500 Hz signal. For a neutron star with 1.2 solar masses, our results exclude maximally strained neutron stars within a 10 pc distance from Earth. Figure 10 also shows that we are more sensitive to neutron stars with lower masses, as previously discussed by Horowitz (2010).

The considerations above must be taken with a grain of salt because the maximum quadrupole is highly dependent on the star’s unknown formation history, its equation of state, and the breaking strain and shear module of the elastic crust. Furthermore, if the neutron star contains exotic states of matter, the maximum quadrupole moment could be higher (Owen 2005). For the fiducial value of the moment of inertia of 10^{38} kg m^2 , the quadrupoles of Gittins & Andersson (2021) correspond to relatively low ellipticities of $\sim 10^{-8}$, and this results in a limited reach in Figure 10.

If the continuous gravitational waves are emitted by r -modes, apart from a weak dependence on the degree of central condensation of the star, their amplitude is

$$\alpha = 0.028 \left(\frac{h_0}{10^{-24}} \right) \left(\frac{d}{1 \text{ kpc}} \right) \left(\frac{1.4 M_\odot}{M} \right) \times \left(\frac{11.7 \text{ km}_\odot}{R} \right)^3 \left(\frac{100 \text{ Hz}}{f_0} \right)^3. \quad (9)$$

From this equation, we derive upper limits on the r -mode amplitude corresponding to different equations of state, in the

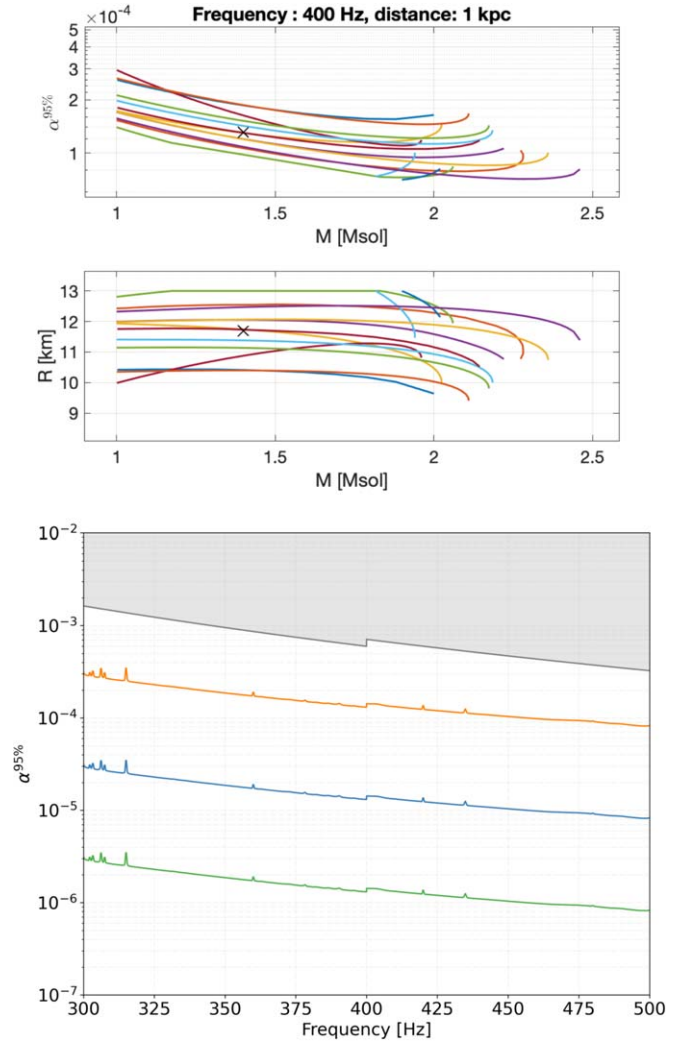


Figure 11. Upper limits $\alpha^{95\%}$ on the r -mode amplitude at the 95% confidence level. Top plot: upper limit as a function of the neutron star mass, where we assume $f = 400$ Hz and a distance to the source of 1 kpc. We consider different equations of state to give an idea of the range of variability of the constraints as a function of the unknown mass and radius of the source. Middle plot: mass–radius combinations corresponding to the considered equations of state. The cross indicates the nominal mass and radius values often used of $M = 1.4 M_\odot$ and $R = 11.7$ km (see Equation (9)). The equations of state are taken from Özel & Freire (2016), <http://xtreme.as.arizona.edu/NeutronStars/index.php/dense-matter-eos>, with $M \in [1, 3] M_\odot$, $R \in [8, 13]$ km, and only ones with a maximum mass lower than $1.9 M_\odot$ are included (Antoniadis et al. 2013; Hebeler et al. 2013; Kurkela et al. 2014; Cromartie et al. 2019). Bottom plot: upper limit as a function of the signal frequency f_0 for sources at 1 kpc (upper orange curve), 100 pc (middle blue curve), and 10 pc (green bottom curve), having assumed $M = 1.4 M_\odot$ and $R = 11.7$ km. The upper shaded gray area shows the region where this search is not sensitive.

range $\alpha^{95\%} \in [3 \times 10^{-4}, 7 \times 10^{-5}]$ at 400 Hz for sources within a distance of 1 kpc; see Figure 11. The range of theoretical predictions in the literature on r -mode amplitudes is $\alpha \sim 8 \times 10^{-7} - 10^{-4}$ (Gusakov et al. 2014a, 2014b) or $\alpha \sim 10^{-5}$ (Bondarescu et al. 2007).

Maccarone et al. (2022) have argued that within 1 kpc there should exist a substantial galactic population of fast-rotating neutron stars in qLMXBs. This is intriguing because Kantor et al. (2021), Gusakov et al. (2014a), and Chugunov et al. (2014) have suggested the existence of a class of hot fast-rotating nonaccreting neutron stars that look very much like

qLMXBs (HOFNARs) that would support very long-lasting r -modes. Our searches begin to probe such hypotheses.

5. Conclusions

In this paper we have presented the most sensitive search to date for continuous gravitational waves from unknown neutron stars in binary systems, with gravitational-wave frequencies between 300 and 500 Hz and orbital periods between 15 and 60 days. We have not detected any astrophysical signal, and we provide the most constraining upper limits in this region of parameter space, improving on existing upper limits by more than an order of magnitude. At spin periods near 4 ms and distances between 10 and 100 pc, we are approximately within one order of magnitude of the minimum ellipticity value of $O(10^{-9})$ proposed by Woan et al. (2018). In this frequency range, a factor of 10 improvement in sensitivity is expected with data from the next generation of detectors. Before these come online a factor of a few may be gained with longer coherent segment lengths—which our new BinarySkyHou \mathcal{F} enables.

Our r -mode amplitude upper limits are well within the range of saturation values for sources up to 1 kpc over the entire frequency range and begin to probe the existence of galactic HOFNARs.

The amplitude of continuous gravitational waves depends on the square of the frequency, while the noise floor of the detectors increases with a lower power of the frequency, thus making higher-frequency searches particularly interesting. On the other hand, for neutron stars in unknown binary systems, the resolution in parameter space increases with at least the fifth power of the frequency, making high-frequency searches a real challenge. These results demonstrate that it is now possible to explore the high-frequency range at interesting sensitivity depths.




The authors thank the scientists, engineers, and technicians of LIGO, whose hard work and dedication produced the data that made this search possible.

We thank Benjamin Steltner for the application of the gating method to the analyzed data set, and Nils Andersson and Fabian Gittins for helpful comments and for the data used to produce Figure 10. This work has utilized the ATLAS cluster computing at MPI for Gravitational Physics Hannover. B.J.O.’s research for this work was supported by NSF grant No. PHY-1912625.

This research has made use of data or software obtained from the Gravitational Wave Open Science Center ([gw-openscience.org](https://gwopenscience.org)), a service of LIGO Laboratory, the LIGO Scientific Collaboration, the Virgo Collaboration, and KAGRA (Abbott et al. 2021e). LIGO Laboratory and Advanced LIGO are funded by the United States National Science Foundation (NSF) as well as the Science and Technology Facilities Council (STFC) of the United Kingdom, the Max-Planck-Society (MPS), and the State of Niedersachsen/Germany for support of the construction of Advanced LIGO and construction and operation of the GEO600 detector. Additional support for Advanced LIGO was provided by the Australian Research Council. Virgo is funded, through the European Gravitational Observatory (EGO), by the French Centre National de Recherche Scientifique (CNRS), the Italian Istituto Nazionale di Fisica Nucleare (INFN) and the Dutch Nikhef, with contributions by institutions from Belgium, Germany, Greece,

Hungary, Ireland, Japan, Monaco, Poland, Portugal, Spain. The construction and operation of KAGRA are funded by Ministry of Education, Culture, Sports, Science and Technology (MEXT), and Japan Society for the Promotion of Science (JSPS), National Research Foundation (NRF) and Ministry of Science and ICT (MSIT) in Korea, Academia Sinica (AS) and the Ministry of Science and Technology (MoST) in Taiwan.

ORCID iDs

P. B. Covas  <https://orcid.org/0000-0002-1845-9309>
M. A. Papa  <https://orcid.org/0000-0002-1007-5298>
R. Prix  <https://orcid.org/0000-0002-3789-6424>
B. J. Owen  <https://orcid.org/0000-0003-3919-0780>

References

- Aasi, J., Abbott, B.P., Abbott, R., et al. 2014, *PhRvD*, **90**, 062010
- Aasi, J., Abbott, P.B., Abbott, R., et al. 2015, *CQGra*, **32**, 074001
- Abbott, B., Abbott, R., Adhikari, R., et al. 2007, *PhRvD*, **76**, 042001
- Abbott, R., Abe, H., Acernese, F., et al. 2021a, *arXiv:2111.13106*
- Abbott, R., T. D. Abbott, T.D., Abraham, S., et al. 2021b, *ApJ*, **922**, 71
- Abbott, R., Abbott, T. D., Acernese, F., et al. 2021c, *arXiv:2111.15116*
- Abbott, R., Abbott, T.D., Abraham, S., et al. 2021d, *PhRvD*, **103**, 064017
- Abbott, R., Abbott, T.D., Abraham, S., et al. 2021e, *SoftX*, **13**, 100658
- Abbott, R., Abe, H., Acernese, F., et al. 2022a, *arXiv:2201.00697*
- Abbott, R., Abbott, T.D., Acernese, F., et al. 2022b, *PhRvD*, **105**, 022002
- Allen, B., & Mendell, G. 2004, SFT (Short-Time Fourier Transform) Data Format Version 2 Specification T040164, <https://dcc.ligo.org/LIGO-T040164/public>
- Andersson, N. 1998, *ApJ*, **502**, 708
- Andersson, N., Kokkotas, K. D., & Stergioulas, N. 1999, *ApJ*, **516**, 307
- Antoniadis, J., Freire, P. C. C., Wex, N., et al. 2013, *Sci*, **340**, 6131
- Ashok, A., Beheshtipour, B., Papa, M.A., et al. 2021, *ApJ*, **923**, 85
- Ashton, G., Keitel, D., Prix, R., & Tenorio, R. 2020, *PyFstat*, Zenodo, doi:10.5281/zenodo.3967045
- Behnke, B., Papa, M. A., & Prix, R. 2015, *PhRvD*, **91**, 064007
- Bondarescu, R., Teukolsky, S. A., & Wasserman, I. 2007, *PhRvD*, **76**, 064019
- Bondarescu, R., Teukolsky, S. A., & Wasserman, I. 2009, *PhRvD*, **79**, 104003
- Bondarescu, R., & Wasserman, I. 2013, *ApJ*, **778**, 9
- Chugunov, A. I., Gusakov, M. E., & Kantor, E. M. 2014, *MNRAS*, **445**, 385
- Covas, P. B., & Prix, R. 2022, *arXiv:2203.08723*
- Covas, P. B., & Sintes, A. 2020, *PhRvL*, **124**, 191102
- Covas, P. B., & Sintes, A. M. 2019, *PhRvD*, **99**, 124019
- Cromartie, H., Fonseca, E., Ramson, S.M., et al. 2019, *NatAs*, **4**, 72
- Cutler, C., & Schutz, B. F. 2005, *PhRvD*, **72**, 063006
- Dergachev, V., & Papa, M. A. 2021, *PhRvD*, **104**, 043003
- Dreissigacker, C., Prix, R., & Wette, K. 2018, *PhRvD*, **98**, 084058
- Fesik, L., & Papa, M. 2020, *ApJ*, **895**, 11
- Friedman, J. L., & Morsink, S. M. 1998, *ApJ*, **502**, 714
- Gittins, F., & Andersson, N. 2019, *MNRAS*, **488**, 99
- Gittins, F., & Andersson, N. 2021, *MNRAS*, **507**, 116
- Glampedakis, K., & Gualtieri, L. 2018, *Astroph. Space Sci. Lib.*, **457**, 673
- Goetz, E., Neunzert, A., Riles, K., et al. 2021, O3a lines and combs in found in self-gated C01 data, LIGO DCC T2100153, <https://dcc-llo.ligo.org/LIGO-T2100153/public>
- Gusakov, M. E., Chugunov, A. I., & Kantor, E. M. 2014a, *PhRvL*, **112**, 151101
- Gusakov, M. E., Chugunov, A. I., & Kantor, E. M. 2014b, *PhRvD*, **90**, 063001
- Hebeler, K., Lattimer, J. M., Pethick, C. J., & Schwenk, A. 2013, *ApJ*, **773**, 11
- Holgado, A. M., Ricker, P. M., & Huerta, E. A. 2018, *ApJ*, **857**, 38
- Horowitz, C. J. 2010, *PhRvD*, **81**, 103001
- Idrisy, A., Owen, B. J., & Jones, D. I. 2015, *PhRvD*, **91**, 024001
- Jaranowski, P., Krolak, A., Schutz, B.F., et al. 1998, *PhRvD*, **58**, 063001
- Kantor, E. M., Gusakov, M. E., & Dommes, V. A. 2021, *PhRvD*, **103**, 023013
- Keitel, D., Tenorio, R., Ashton, G., & Prix, R. 2021, *JOSS*, **6**, 3000
- Krishnan, B., Sintes, A.M., Papa, M.A., et al. 2004, *PhRvD*, **70**, 082001
- Kurkela, A., Fraga, E. S., Schaffner-Bielich, J., & Vuorinen, A. 2014, *ApJ*, **789**, 127
- Lasky, P. 2015, *PASA*, **32**, E034
- Leaci, P., & Prix, R. 2015, *PhRvD*, **91**, 102003
- Lindblom, L., Owen, B. J., & Morsink, S. M. 1998, *PhRvL*, **80**, 4843

- Maccarone, T. J., Degenaar, N., Tetarenko, B. E., et al. 2022, [MNRAS](#), **512**, 2365
- Ming, J., Papa, M.A., Eggenstein, H.-B., et al. 2022, [ApJ](#), **925**, 8
- Mukherjee, A., Messenger, C., & Riles, K. 2018, [PhRvD](#), **97**, 043016
- Owen, B. J. 2005, [PhRvL](#), **95**, 211101
- Owen, B. J., Lindblom, L., Cutler, C., et al. 1998, [PhRvD](#), **58**, 084020
- Özel, F., & Freire, P. 2016, [ARA&A](#), **54**, 401
- Rajbhandari, B., Owen, B.J., Caride, S., et al. 2021, [PhRvD](#), **104**, 122008
- Reisenegger, A., & Bonacic, A. A. 2003, [PhRvL](#), **91**, 201103
- Singh, N., Haskell, B., Mukherjee, D., & Bulik, T. 2020a, [MNRAS](#), **493**, 3866
- Singh, N., Haskell, B., Mukherjee, D., et al. 2020b, [MNRAS](#), **493**, 3866
- Steltner, B., Papa, M., & Eggenstein, H.-B. 2022, [PhRvD](#), **105**, 022005
- Steltner, B., Papa, M. A., Eggenstein, H. -B., et al. 2021, [ApJ](#), **909**, 79
- Tenorio, R., Keitel, D., & Sintes, A. M. 2021, [Univ](#), **7**, 474
- The LIGO-Virgo Collaboration 2021, The O3a Data Release, doi: [10.7935/nfnt-hm34](#)
- van Eysden, C. A., & Melatos, A. 2008, [CQGra](#), **25**, 225020
- Woan, G., Pitkin, M. D., Haskell, B., Jones, D. I., & Lasky, P. D. 2018, [ApJL](#), **863**, L40
- Yoshida, S., Yoshida, S., & Eriguchi, Y. 2005, [MNRAS](#), **356**, 217
- Zhang, Y., Papa, M.A., Krishnan, B., et al. 2021, [ApJL](#), **906**, L14